Frenkel-Holstein Hamiltonian Applied to Absorption Spectra of Quaterthiophene-based 2D Hybrid Organic-Inorganic Perovskites

Svenja M. Janke[1], Mohammad B. Qarai[2], Volker Blum[1,3], Frank C. Spano[2]

[1] Department of Mechanical Engineering and Materials Science, Duke University, Durham, NC 27708, USA, [2] Chemistry, Temple University, 19122 Philadelphia, PI, USA [3] Department of Chemistry, Duke University, Durham, NC 27708, USA

Abstract

For the prototypical two-dimensional hybrid organic-inorganic perovskites (2D HOIPs) (AE4T)PbX_4 (X = Cl, Br, I) we demonstrate that the Frenkel-Holstein Hamiltonian (FHH) can be applied to describe the absorption spectrum arising from the organic component. We first model the spectra using only the four nearest-neighbor couplings between translationally inequivalent molecules in the organic herringbone lattice as fitting parameters in the FHH. We next use linear-response time-dependent density functional theory (LR-TDDFT) to calculate molecular transition densities, from which all of the extended excitonic couplings are evaluated based on the atomic positions within the 2D HOIPs. We find that both approaches reproduce the experimentally observed spectra, including changes in their shape and peak positions. The spectral changes are correlated to a decrease in excitonic coupling from X = Cl to X = I. Importantly, the LR-TDDFT-based approach with extended excitonic couplings not only gives better agreement with the experimental absorption line shape than the approach using a restricted set of fitted parameters, but also allows us to relate the changes in excitonic coupling to the underlying geometry. We accordingly find that the decrease in excitonic coupling from X = Cl to Br to I is due to an increase in molecular separation, which in turn can be related to the increasing Pb-X bond length from Cl to I. Our research opens up a potential pathway to predicting optoelectronic properties

of new 2D HOIPs from *ab initio* calculations and to gain insight into structural relations from 2D HOIP absorption spectra.

Introduction

Hybrid organic-inorganic perovskites (HOIPs) are experiencing a meteoric rise as new, low-temperature depositable semiconductors, initially due to the remarkable properties of a group of HOIPs as potential solar cell materials[1–9], but currently more broadly as optoelectronic materials for light emitting diodes (LEDs)[10–19], chirality-controlled and/or spin-optoelectronic devices[20–22] and other application areas. For 3D perovskites, only a limited compositional space is accessible, but when the size of the organic cation is increased, the resulting lower-dimensional hybrid perovskites offer superior chemical stability and a vast set of choices of chemically tunable organic cations[23–25]. An organic cation molecule with a low band gap can participate directly in the functionality of the perovskite by partially contributing[26–29] to or entirely forming the frontier levels[11,30,31] of the overall compound, or by accepting excitons from the inorganic framework into emissive organic triplet states[32–37].

Spectroscopically, this leads to strong organic contributions that can overlap with inorganic contributions[31,38]. For the investigation as well as prediction of new 2D HOIPs for, e.g., LED or solar cell application, it is hence necessary to understand the contribution of the organic component to the absorption and emission properties of the perovskite and how the structural properties of the perovskite influence the materials' spectra. Excitonic properties are in principle accessible from the Bethe-Salpeter equation (BSE) or linear-response time-dependent density functional theory (LR-TDDFT)[39] using range-separated hybrid functionals[39–41]. However, in practice, 2D HOIPs with optically active organic cations tend to have large supercells with hundreds of atoms per unit cell due to steric requirements (e.g., need to accommodate rotation of inorganic octahedra versus one another) and/or disorder in the organic and inorganic framework[24,27,28,30]. Without further approximations, this mostly puts them out of reach for current BSE and LR-TDDFT implementations due to their almost prohibitive scaling with number of atoms[39]. Accordingly, to the best of our knowledge, only a handful of studies have employed BSE or LR-TDDFT to investigate excitonic and photophysical properties of 2D HOIPs[42–49]. Even fewer treat organic cations that can contribute to the absorption spectrum in a similar spectral region as the inorganic[50,51]. To exacerbate matters, Frenkel excitons in organic molecules couple strongly to optical phonons derived from intramolecular vibrations.[52,53] While electronic excitations and their interaction

with the underlying nuclear framework are in principle available from LR-TDDFT[48], for rigorous description of excitonic properties at room temperature[54], BSE calculations including treatment of atomic motions would be necessary, which are still in their beginning stages of development[55,56].

Next to *ab initio* methods, photophysical properties can be investigated using phenomenological based model Hamiltonians. One of the earliest models to relate structural trends to optical properties in organic materials was developed by Kasha[57–59] around 1960. It allowed one to classify J- and H-aggregates based on intermolecular Coulomb coupling. For H-aggregates, the intermolecular Coulomb coupling is positive, which is related to a side-by-side orientation of the molecular transition dipole moments and characterized by a blue shift of the broad main absorption band (H band)[52]. Conversely, in J-aggregates, the coupling is negative, corresponding to a head-to-tail orientation and hence a red-shifted, narrow main absorption band. The inclusion of local vibronic couplings, which are prominent in many conjugated organic molecules, can be accomplished using the Frenkel-Holstein Hamiltonian[52,60–63] (FHH), which is similar to the conventional Holstein Hamiltonian[64] and can be further extended to include contributions from intermolecular charge transfer states[52].

The Frenkel-Holstein Hamiltonian has been successfully applied to a wide array of organic crystals and aggregates to describe the influence of vibronic and excitonic couplings, disorder and thermal expansion on spectral line shapes in linear, curved, helical and herringbone aggregates[52,65]. In the latter class, especially acene molecules[66–68] and oligothiophenes[69–76] have been investigated. Interestingly, derivatives of these molecules have also been used as organic components in 2D HOIPs[27,28,30,38,77]. Figure 1a and b show the molecular packing within the organic layer in (AE4T)$PbBr_4$, which is similar to that found in the weakly interacting layers of organic molecules in the crystal phase of acenes[78] and oligothiophenes[79,80]. In these (100)-oriented 2D HOIPs, a mono- or double layer of herringbone-ordered organic molecules is isolated from the next layer by the inorganic component[24,38]. A prototypical example of such a cation in 2D HOIPs is the quaterthiophene (OT4) derivative 5,5’’’-bis(aminoethyl)-2,2’:5’,2’’:5’’,2’’’-quaterthiophene (AE4T) [24]. It was one of the early organic cations employed in 2D HOIPs and has since been used in a number of studies that investigate different structural and photophysical properties of 2D HOIPs[11,24,30,31,38,81–83].

The Frenkel exciton on the organic component and Wannier-Mott exciton on the inorganic component in hybrid materials can couple to each other. In the strong coupling limit[53] when an organic and inorganic state are in resonance, a splitting of a resulting mixed state would be observed that is larger than the dissipative width of both the organic and the inorganic resonant state. In the weak coupling limit, interaction between the organic and inorganic component results in nonradiative energy transfer between the organic and inorganic component[53]. In agreement with this picture and a type-I level alignment[30,31], emission from (AE4T)$PbCl_4$ has been observed from the organic component after excitation of the inorganic component[11,31,38,83]. For (AE4T)$PbBr_4$ and (AE4T)PbI_4, a type II level alignment has been suggested, where excited charge carriers can be transferred as separated electrons or holes between organic and inorganic components[30,31].

Overall, the (AE4T)PbX_4 based HOIPs and their absorption spectra appear to present an ideal model system for taking the first steps in adapting the Frenkel-Holstein Hamiltonian to 2D HOIPs to model their photophysical properties. In this paper, we demonstrate that experimental trends in the organic absorption spectra of the 2D (AE4T)PbX_4 (X= Cl, Br, I) HOIPs can be well reproduced within the framework of the FHH. We first demonstrate the principle by fitting the FHH to experimental absorption spectra using only excitonic nearest neighbor couplings between translationally inequivalent molecules in the herringbone lattice. In a second step, we calculate extended excitonic couplings from LR-TDDFT instead of fitting them, using the atomic positions of the organic molecules in the (AE4T)PbX_4 HOIPs as input and showing that this procedure gives an excellent description of the absorption spectra. We demonstrate that trends observed for the experimental absorption spectra of the organic component are a result of decreasing excitonic coupling from X = Cl to X = I and caused by the confining influence of the inorganic framework. Our research opens up a new pathway to investigate optoelectronic properties of 2D HOIPs and to gain insight into structural relations from 2D HOIP absorption spectra.

Methods

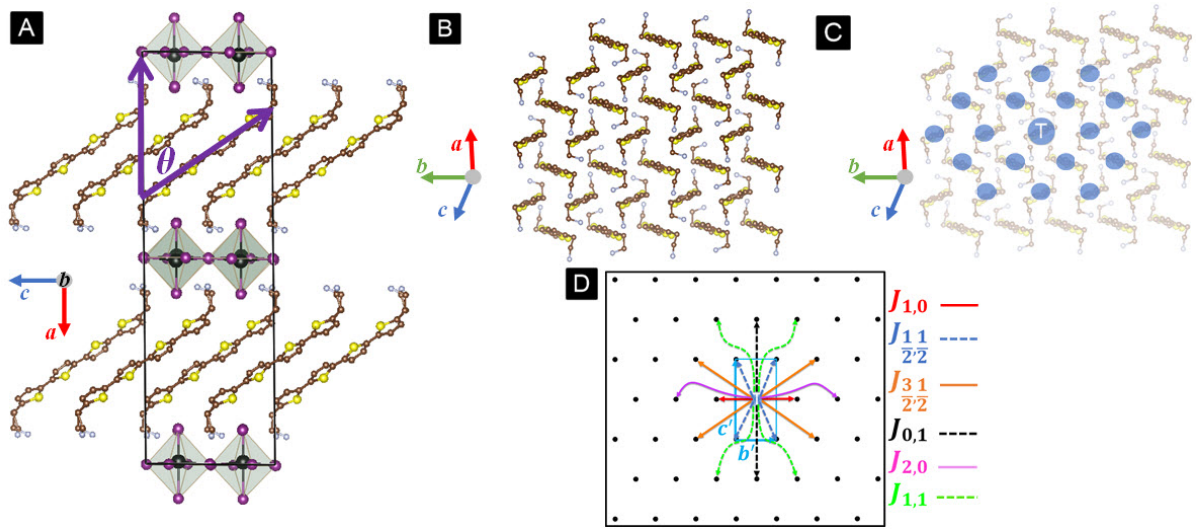

Figure 1: a) Structure of (AE4T)$PbBr_4$ based on Ref.s[30,38]. Inorganic sheets are formed by Pb-Br octahedra and separated by AE4T molecules. The molecular tilt angle θ (purple) is the angle between the AE4T molecular plane with the normal vector to the $\boldsymbol{b}$, $\boldsymbol{c}$ plane of the inorganic sheets. Each molecular plane contains four molecules per unit cell. b) Within a layer and viewed along the molecular tilt angle θ, the organic molecules assume a herringbone pattern. c) For simulations with the Frenkel-Holstein Hamiltonian, we assume a simplified lattice where each chromophore is equivalent to its neighboring chromophores and identified by its center-of-mass (blue circles). d) Additionally, we use a simplified lattice with two molecules per unit cell (blue box), half the size of the original unit cell in a). To distinguish from the original unit cell in a) we denote the simplified unit cell vectors as $\boldsymbol{b}'$ and $\boldsymbol{c}'$ with $\boldsymbol{c}' = \boldsymbol{c}$ and $\boldsymbol{b}' = \frac{1}{2}\boldsymbol{b}$. For AE4T, the two nearest neighbor couplings are $J_{-1,0} = J_{1,0}$ (red) and the four 2nd nearest neighbor coupling are $J_{1/2,1/2} = J_{-1/2,1/2} = J_{1/2,-1/2} = J_{-1/2,-1/2}$ (dashed blue). Couplings up to the 6th nearest neighbor are also shown.

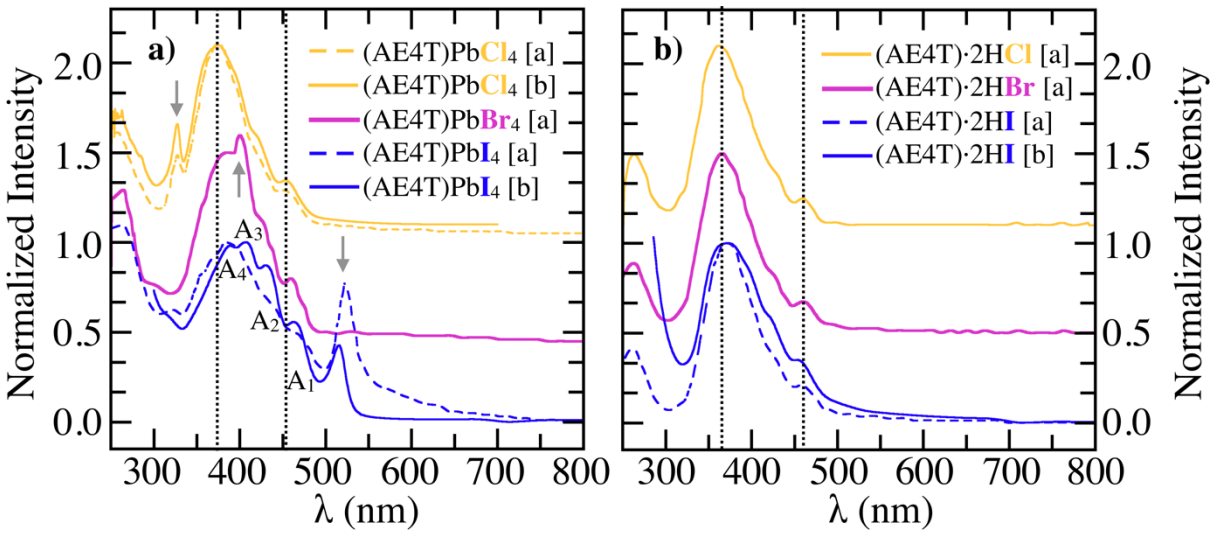

Figure 2: Room temperature UV-vis absorption spectra a) of (AE4T)PbX_4 with X = Cl (yellow), Br (purple) and I (blue) normalized to the peaks of the organic absorption spectra (H band) and with shifted baselines for visual clarity. The excitonic peaks on the inorganic components are indicated by grey arrows. The dashed perpendicular lines indicate the position of the first peak (A_1) and H band (A_4 peak) of (AE4T)$PbCl_4$. Exemplary for (AE4T)PbI_4, the peaks are labeled according to their expected vibrational transition, starting with the transition A_1 from the vibrational ground state in the electronic ground state S_0 to the vibrational ground state in the first electron excited state (S_1), to A_4 for the transition from the vibrational ground state to the third vibrationally excited state of the first electronically excited state. The broad features in the absorption spectra due to absorption from the organic component red-shift from Cl to I. b) Absorption spectra of thin film (AE4T)·2HX with X= Cl (yellow), Br (purple) and I (blue). The thin film absorption spectra for X = Cl and Br are almost identical, but slightly blue-shifted for X = I. Spectra adapted with permission from Ref.[38]. Copyright 1999 American Chemical Society (marked as [a]), and adapted from Ref.[31] with permission from the Royal Society of Chemistry (marked as [b]).

A. Absorption spectra

The room temperature UV-vis absorption spectra of thin film (AE4T)PbX_4 and (AE4T)·2HX were measured in the group of David B. Mitzi in 1999[38] and 2019[31]. We obtained the experimental absorption

spectra by extracting absorption intensity in steps of 1 nm from the absorption spectra plotted in Ref.[38] with the Engauge Digitizer[84] software. The (AE4T)$PbCl_4$, (AE4T)PbI_4 and (AE4T)·2HI films have recently been remeasured in Ref.[31] and we retrieved the dataset of the respective measurements from their entries in the HybriD^3 database[85] (materials No. 2 and No. 22) or from the authors (for the (AE4T)·2HI film). Figure 2a and b show the absorption spectra of the (AE4T)PbX_4 perovskites and (AE4T)·2HX films. In general, the 1999[38] and 2019[31] absorption spectra from both references are in good agreement with respect to the positions of peaks and shoulders. The intensities of the spectral peaks and shoulders between the two studies agree well for (AE4T)$PbCl_4$ and relatively well for (AE4T)·2HI, but not for (AE4T)PbI_4. For (AE4T)PbI_4, the absorption spectrum from 1999 peaks at the fourth peak (385 nm, A_4, see Figure 2) of the vibronic progression, whereas the absorption spectrum measured in 2019 peaks at the third peak (408 nm, A_3) of the vibronic progression. The disagreement, however, is minor in so far as the overall positions of the shoulders in the vibronic progression between the two measurements are roughly the same, and in so far as the A_3 (408 nm) and A_4 (384 nm) peaks have similar intensities for the spectrum measured in 2019. For adjusting the chosen nearest neighbor coupling in the Frenkel-Holstein Hamiltonian and determining the dielectric constant ε_r, we relied on the remeasured absorption spectra from Ref.[31] where possible to avoid residual errors due to interpolating the absorption spectra from printed plots and because the shoulders of the vibronic progression are more clearly identifiable for (AE4T)PbI_4 in Ref.[31]. Positions of A_1 peaks and the maxima of the organic absorption spectra were extracted by determining maxima in the absorption intensity and are listed in Table S1 of the supplementary material.

B. Atomic Structure

Experimentally, the crystal structure of (AE4T)$PbBr_4$ was obtained by Mitzi and co-workers using x-ray crystallography[38] while only the unit cell parameters were determined for (AE4T)PbI_4[30,38]. To calculate the excitonic couplings up to the 6th neighbors of the organic layer, we rely on the theoretical structures obtained by Liu *et al.*[30], available on the HybriD^3 database[85], materials No. 21 ((AE4T)$PbCl_4$), No. 3 ((AE4T)$PbBr_4$) and No. 22 ((AE4T)PbI_4). Based on the (AE4T)$PbBr_4$ crystal structure, Liu *et al.*[30] resolved the disorder in the experimental structure and performed density functional theory

structure geometry relaxations using the Perdew-Burke-Ernzerhof functional[86] with Tkatchenko-Scheffler pairwise dispersion correction[87] (DFT-PBE+TS) within the all-electron electronic structure code FHI-aims[88]. Validation of their prediction quality for the geometry was performed against the experimentally well-known 3D Methylammonium lead iodide orthorhombic phase. Liu *et al.* obtained structures for (AE4T)PbI_4 and (AE4T)$PbCl_4$ by replacing Br in (AE4T)$PbBr_4$ with I and Cl, respectively, followed by DFT-PBE+TS geometry relaxation. For the Br- and I-based compounds, they achieved very good agreement with the experimental measurements[30]. For the Cl-based compound, the ***a***-lattice parameter is known and underestimated by the theoretical structure[31].

Figure 1a shows the atomic structure of (AE4T)$PbBr_4$[30,38], analogous to the structure used below for the Cl- and I-based compounds. Inorganic sheets of Pb-X-octahedra are separated by a layer of organic AE4T molecules. Within the organic layer (Figure 1b), the AE4T molecules assume a herringbone packing arrangement. To describe the interaction of a specific target chromophore T (Figure 1c) with the neighboring chromophores within the Frenkel-Holstein Hamiltonian, we assume a simplified lattice with structurally equivalent chromophores that are identified by their center-of-mass. We describe the interactions of each chromophore with its neighbors (Figure 1d), ranging from the two nearest neighbor interactions ($J_{\pm1,0}$, red) to the four 6th nearest neighbor interactions ($J_{\pm1,\pm1}$, dashed green). Couplings with fractional indices refer to chromophores with different orientation than the target chromophore in the herringbone structure.

We consider only interaction within the organic herringbone layers and not between the organic layers, in line with previous treatment of oligothiophene crystals[70]. Exemplary computation of the nearest neighbor interaction between two chromophores in neighboring herringbone planes (see Figure S1 in the supplementary material) showed that the magnitude of the between-layer interaction is by about a factor of 10 smaller than nearest neighbor interaction within the herringbone planes when the same dielectric screening of $\varepsilon = 2.8$ is applied to both of them. Additionally, the coupling between organic layers would be even further reduced due to the screening from the inorganic layer where the dielectric constant ε is expected to be higher than that for the organic[24].

For the (AE4T)·2HX films, no structural information is available. We assume that the molecules also form a herringbone pattern similar to that inside the (AE4T)PbX_4 perovskites as has been observed for quaterthiophene[79,80].

C. The Frenkel-Holstein Hamiltonian

In order to model the absorption spectrum of the organic layers in the (AE4T)PbX_4 perovskites and the (AE4T)·2HX films, we need to express the Frenkel-Holstein Hamiltonian $\widehat{H}_{\mathrm{FH}}$[52] for a 2D herringbone lattice. For this, we model a single layer of organic molecules and neglect the presence of the inorganic framework. The unit cell of the (AE4T)PbX_4 perovskites contains four organic molecules per layer, two of which are roughly translationally equivalent to the other two if the aminoethyl-linker group is neglected. Because the linker group does not contribute to the chromophoric system, for the simulations with the FHH we choose a unit cell that contains two chromophores (blue rectangle, Figure 2d) with the lattice vectors $\boldsymbol{b}'$and $\boldsymbol{c}'$ that relate to the original lattice vectors $\boldsymbol{b}$ and $\boldsymbol{c}$ of the 2D HOIP as $\boldsymbol{b}' = \frac{1}{2}\boldsymbol{b}$ and $\boldsymbol{c}' = \boldsymbol{c}$. A lattice contains $N_{\mathrm{h}} = 2\ (N_{b'} \times N_{c'})$ chromophores, where $N_{b'}$ is the number of unit cells along the $\boldsymbol{b}'$axis and $N_{c'}$ is the number of unit cells along the $\boldsymbol{c}'$ axis. The lattice can be divided into two sublattices that each contain translationally equivalent molecules. Accordingly, the position vector for a molecule in the first sublattice is given by

$$\boldsymbol{R_1} = n_{\mathrm{b}'}\,\boldsymbol{b}' + n_{\mathrm{c}'}\,\boldsymbol{c}' \tag{1}$$

with $n_{b'}(n_{c'}) = 0, 1, 2, \ldots, N_{b'} - 1(N_{c'} - 1)$, while the position vector for a molecule in the second sublattice is given by

$$\boldsymbol{R_2} = \left(n_{\mathrm{b}'} + \frac{1}{2}\right)\boldsymbol{b}' + \left(n_{\mathrm{c}'} + \frac{1}{2}\right)\boldsymbol{c}'. \tag{2}$$

In this 2D-herringbone lattice, the Frenkel-Holstein Hamiltonian is expressed as

$$\hat{H}_{\mathrm{FH}} = \hat{H}_{\mathrm{el}} + \hat{H}_{\mathrm{vib}}. \tag{3}$$

where the *electronic* $\hat{H}_{\mathrm{el}}$ and *vibronic* $\hat{H}_{\mathrm{vib}}$ terms are

$$\hat{H}_{\mathrm{el}} = \hbar\omega_{0-0} + D + \sum_{\boldsymbol{\sigma}=\mathbf{1},\mathbf{2}} \sum_{\boldsymbol{R_\sigma}} \sum_{\boldsymbol{s}} J_{\boldsymbol{s}} \, |\boldsymbol{R_\sigma}\rangle\langle\boldsymbol{R_\sigma} + \boldsymbol{s}| \tag{4}$$

and

$$\hat{H}_{\mathrm{vib}} = \hbar\omega_0 \sum_{\boldsymbol{\sigma}=\mathbf{1},\mathbf{2}} \sum_{\boldsymbol{R_\sigma}} b^{\dagger}_{\boldsymbol{R_\sigma}} b_{\boldsymbol{R_\sigma}} + \hbar\omega_0\lambda \sum_{\boldsymbol{\sigma}=\mathbf{1},\mathbf{2}} \sum_{\boldsymbol{R_\sigma}} \left(b^{\dagger}_{\boldsymbol{R_\sigma}} + b_{\boldsymbol{R_\sigma}}\right) |\boldsymbol{R_\sigma}\rangle\langle\boldsymbol{R_\sigma}| + \hbar\omega_0\lambda^2. \tag{5}$$

In Eq. (4), $\omega_{0\text{-}0}$ is the gas-phase transition energy of the monomer, which is shifted by D, the gas-phase-to-crystal shift, as a result of nonresonant intermolecular interactions. $J_{\boldsymbol{s}}$ is the (resonant) excitonic coupling between the chromophores located at $\boldsymbol{R_\sigma}$ and $\boldsymbol{R_\sigma} + \boldsymbol{s}$, which is taken to be independent of $\boldsymbol{R_\sigma}$. The electronic operator $|\boldsymbol{R_\sigma}\rangle\langle\boldsymbol{R_\sigma} + \boldsymbol{s}|$ annihilates an electronic excitation on chromophore $\boldsymbol{R_\sigma} + \boldsymbol{s}$ and creates an excitation on molecule $\boldsymbol{R_\sigma}$. Here, the index $\boldsymbol{R_\sigma}$ runs over all chromophores in sublattice σ (=1,2) and $\boldsymbol{s}$ is the distance vector between $\boldsymbol{R_\sigma}$ and any other chromophore in the lattice (either in the same sublattice or in the other sublattice). Based on the arrangement of the chromophores in the 2D HOIP (Figure 1d), the excitonic coupling $J_{\boldsymbol{s}}$ for the nearest neighbors are defined by distance vectors $\boldsymbol{s} = 1\boldsymbol{b'} + 0\boldsymbol{c'}$ and $\boldsymbol{s} = -1\boldsymbol{b'} + 0\boldsymbol{c'}$. $\boldsymbol{s}$ may be equivalently denoted by its components along $\boldsymbol{b'}$ and $\boldsymbol{c'}$, e.g. "1,0", "−1,0", etc. Due to the symmetry of the lattice, $J_{1,0} = J_{-1,0}$ (Figure 1d, red). Correspondingly, for the four second nearest neighbors $\boldsymbol{s} = \pm 1/2\,\boldsymbol{b'} \pm 1/2\;\boldsymbol{c'}$ and $J_{1/2,1/2} = J_{-1/2,1/2} = J_{1/2,-1/2} = J_{-1/2,-1/2}$ (Figure 1d, dashed blue), etc.

In Eq. (5), the aromatic-quinoidal stretching mode, which dominates the vibronic coupling, has a frequency denoted ω_0. The corresponding ground and excited state (harmonic) nuclear potentials are shifted relative to each other since the excited state has more quinoidal character. The shift gives rise to local vibronic coupling represented by the second term in Eq. (5). The shift is quantified by the

dimensionless Huang-Rhys factor λ^2. $b^{\dagger}_{\boldsymbol{R_\sigma}}$ and $b_{\boldsymbol{R_\sigma}}$ are field operators that create and annihilate, respectively, one vibrational quantum in the ground state harmonic well of the chromophore at $\boldsymbol{R_\sigma}$.

The eigenstates of the Frenkel-Holstein Hamiltonian can be expressed using a multi-particle basis set[89,90]. Consistent with the translational symmetry inherent in our simplified 2D crystal, the wave function is expressed as a linear combination of delocalized single- and two-particle states characterized by a wave vector $\boldsymbol{k}$[66]

$$\left|\psi^{\delta,\boldsymbol{k}}\right\rangle = \sum_{\sigma}\sum_{\tilde{\nu}} C^{\delta}_{\boldsymbol{k},\tilde{\nu}} |\boldsymbol{k}\sigma,\tilde{\nu}\rangle + \sum_{\sigma}\sum_{\tilde{\nu}}\sum_{\boldsymbol{s}}\sum_{\nu} C^{\delta}_{\boldsymbol{k}\sigma,\tilde{\nu};\nu} |\boldsymbol{k}\sigma,\tilde{\nu};\boldsymbol{s},\nu\rangle\,. \tag{6}$$

Here, $\delta = 1, 2, 3, \ldots$ labels the eigenstate with a given wave vector $\boldsymbol{k}$. The delocalized symmetry-adapted one- and two-particle states are defined as:

$$|\boldsymbol{k}\sigma,\tilde{\nu}\rangle = \frac{1}{N}\sum_{\boldsymbol{R_\sigma}} \mathrm{e}^{i\boldsymbol{k}\boldsymbol{R_\sigma}} |\boldsymbol{R_\sigma},\tilde{\nu}\rangle\,. \tag{7}$$

and

$$|\boldsymbol{k}\sigma,\tilde{\nu};\boldsymbol{s},\nu\rangle = \frac{1}{N}\sum_{\boldsymbol{R_\sigma}} \mathrm{e}^{i\boldsymbol{k}\boldsymbol{R_\sigma}} |\boldsymbol{R_\sigma},\tilde{\nu};\boldsymbol{R_\sigma}+\boldsymbol{s},\nu\rangle\,. \tag{8}$$

The single-particle contributions $\left|\boldsymbol{R_\sigma},\tilde{\nu}\right\rangle$ in Eq. (7) describe an electronically excited chromophore $\boldsymbol{R_\sigma}$ with $\tilde{\nu}$ quanta in its shifted excited nuclear potential. In two-particle excitations $|\boldsymbol{R_\sigma},\tilde{\nu};\boldsymbol{R_\sigma}+\boldsymbol{s},\nu\rangle$, the vibronically excited chromophore $\boldsymbol{R_\sigma}$ has $\tilde{\nu}$ quanta in its shifted excited-state nuclear potential, while chromophore $\boldsymbol{R_\sigma}+\boldsymbol{s}$ is in its ground electronic state but with $\nu > 0$ vibrational quanta in its unshifted nuclear potential. Three-particle contributions were shown to have only a negligible effect on absorption or emission spectra[90]. Once the eigenvalues $\left|\psi^{\delta,\boldsymbol{k}}\right\rangle$ have been calculated by diagonalizing the Frenkel-Holstein Hamiltonian $\widehat{H}_{\mathrm{FH}}$, the absorption spectrum normalized to the total number of chromophores can be simulated using[52,65]:

$$I_{\mathrm{org}}(\omega) = \frac{1}{N_h\mu^2}\sum_{\delta}\omega^{(\delta)}\left|\left\langle\psi^{\delta,\boldsymbol{k}=0}\left|\hat{\mu}\right|G\right\rangle\right|^2\Gamma\left(\omega-\omega^{(\delta)}\right), \tag{9}$$

where the absorption intensity I_{org} is a function of the frequency ω, μ is the transition dipole moment and $\hat{\mu}$ the dipole moment operator. $\omega^{(\delta)}$ is the δth eigenvalue of the Frenkel-Holstein Hamiltonian. The sum contains the product of the oscillator strength $\omega^{(\delta)}\left|\left\langle\psi^{\delta,\boldsymbol{k}=\mathbf{0}}\left|\hat{\mu}\right|G\right\rangle\right|^2$ for the transition between the ground state $|G\rangle$ and an eigenstate $\left|\psi^{\delta,\boldsymbol{k}=\mathbf{0}}\right\rangle$ of the Frenkel-Holstein Hamiltonian multiplied by a Gaussian broadening function $\Gamma(\omega) = \exp\left(-\omega^2/(2\Delta\omega^2)\right)$ with a broadening of $\Delta\omega = 0.6\,\hbar\omega_0$ chosen here. Before proceeding we note that the $\boldsymbol{k}$=0 excitons from each sublattice can generally combine to form two Davydov components. However, as the relative angle between the two transition dipole moments within a unit cell is practically zero (< 3° using LR-TDDFT calculated transition charges, see section E below**)** the lower-energy Davydov component is not observed in the absorption spectrum[70].

For the present calculations, we assume a lattice consisting of two (6×3) sublattices amounting to a total of 36 chromophores within periodic boundary conditions. We further cap the total number of vibrational quanta in the one- and two-particle states to be four. As demonstrated in Figure S2 the supplementary material, the shape of the absorption spectrum is well converged for both choices. In AE4T and its structural basic form quaterthiophene, the dominant vibration of the organic molecule corresponds to the symmetric vinyl-stretching mode with $\hbar\omega_0 = 1440$ cm^{-1} [38,91]. The symmetric vibration is largely due to an oscillation between aromatic and quinoidal forms in the quaterthiophene backbone. The Huang-Rhys factor λ^2 can be obtained from the ratio in intensities of the A_1 and A_2 peak in the vibronic progression of the monomer spectrum[52]. For our simulations of AE4T, we assume that the Huang-Rhys factor is the same for OT4 and AE4T due to their structural similarities. Accordingly, we use the experimental emission spectrum of OT4 monomer[92] to determine the Huang-Rhys factor and find $\lambda^2 = 1.25$, in good agreement with $\lambda^2 = 1.35$ determined previously for OT4[93] (see Figure S3 in the supplementary material). We determine $D + \hbar\omega_{0-0}$ from the A_1 peak of the experimental absorption spectrum. The corresponding values for the experimental absorption spectra and the Frenkel-Holstein Hamiltonian models used here are listed in Table S1.

We follow two strategies to obtain the excitonic coupling $J_{\boldsymbol{s}}$ described in more detail below. For the first approach (called 'fitted model' hereafter), we adjust the excitonic couplings, $J_{\pm1/2,\pm1/2}$, to fit the

experimental absorption spectra relying on a fitting procedure. For the second approach (called 'calculated model' hereafter), we obtain excitonic coupling constants for up to 6th nearest neighbors from LR-TDDFT calculated transition densities based on the atomic structures for (AE4T)PbX_4 from Ref.[30,31] to relate the trends in the excitonic coupling constants to underlying geometrical properties.

D. Fitting Procedure for Fitted Model

To find the best representation of the experimental absorption spectra of the organic part for (AE4T)PbX_4 and of (AE4T)·2HX, we retain only the four couplings $J_{\pm1/2,\pm1/2}$ (Figure 1d, dashed blue) which are assumed to be equal. We then treat $J_{\pm1/2,\pm1/2}$ as a fitting parameter. We note that although the four couplings are second nearest neighbors, they provide a superior fit over that based on the two actual nearest neighbors ($J_{1,0}$ and $J_{-1,0}$). A fit based on the four interactions $J_{\pm1/2,\pm1/2}$ reflects the 2D nature of the AE4T layers, whereas the two nearest neighbor interactions $J_{1,0}$ and $J_{-1,0}$ reflect a 1D chain. However, we show in Table S2 and S3 of the supplementary material that similar trends are obtained when fitting either the four interactions ($J_{\pm1/2,\pm1/2}$) or two ($J_{\pm1,0}$) nearest neighbor interactions.

For the fit, we vary $J_{\pm1/2,\pm1/2}$ from 0.05 ω_0 to 0.65 ω_0 in steps of 0.01 ω_0. We identify the most suitable excitonic coupling constant to fit the experimental absorption spectra by modifying an implementation of the Pendry reliability factor[94] (R-factor) R_P distributed with Refs.[95,96]. The Pendry R-factor was originally designed to calculate the match between experimental and theoretical low energy electron diffraction spectra while being relatively insensitive to discrepancies in the intensity[94]:

$$R_P = \int d\lambda \frac{\left(Y_{th} - Y_{exp}\right)^2}{\left(Y_{th}^2 + Y_{exp}^2\right)} \quad (10)$$

In discretized form, dλ becomes the spacing between data points in the absorption spectra (here, dλ = 1 nm, the step with which the experimental spectra were recorded or extrapolated). Y_{th} and Y_{exp} are

calculated from a Lorentzian distribution using renormalized logarithmic derivatives of the intensities and the approximate half width at half maximum (γ) of the peaks in the spectrum[94,96]:

$$Y(\lambda) = \frac{L^{-1}(\lambda)}{L^{-2}(\lambda) + \gamma^2} \tag{11}$$

$L(\lambda) = I'(\lambda)/I(\lambda)$ is given by the intensity $I(\lambda)$ and its first derivative $I'(\lambda)$.[96,97] We found γ = 16 nm to be optimal. The implementation finds the best R_P by shifting the theoretical spectrum with respect to the experimental one within a predefined range. To facilitate the initial guess, we shift the absorption spectrum calculated with the Frenkel-Holstein Hamiltonian so that the A_1 peak matches the experimentally obtained A_1 peak and allow a shift of ±10 nm. For the fit, we only consider the data of the immediate region surrounding the organic band in the absorption spectrum to avoid fitting contributions in the experimental absorption spectrum that are not modeled by the Frenkel-Holstein Hamiltonian (i.e. onset of higher electronic transitions or noise in the spectrum). Finally, for (AE4T)PbX_4, we modified the implementation of Refs.[95–97] to add or subtract a Gaussian peak to account for the inorganic exciton peak, which is not part of the simulated FHH but which is of course present in the experimental absorption spectra (vide infra).

E. Calculation of Excitonic Coupling

For the 'calculated model' (as opposed to the 'fitted model'), we determined the excitonic couplings for nearest neighbors and beyond based on Coulomb couplings between transition charges of the monomers in the framework of molecular exciton theory[98,99]. Transition densities were obtained for a single AE4T molecule where the functional groups were replaced by CH_3 groups by linear-response time-dependent density functional theory (LR-TDDFT) calculations using the long-range corrected ωB97 hybrid functional[100] and the def2SVP basis set[101] within Gaussian09. The transition charges were then projected onto the molecular atoms using Mulliken population analysis[99]. In the limit of weakly interacting molecules, short range interactions due to overlap of the molecular wave functions like charge transfer and exchange (i.e. excitation of electrons between two molecules) can be

neglected[102,103], and the excitonic coupling between the molecules (i.e. well-localized Frenkel excitons) can then be described as Coulomb coupling between the transition charges q_i^{t} and q_j^{t}[99,104]:

$$J_{\boldsymbol{s}} = \frac{1}{4\,\pi\varepsilon_0\varepsilon_{\mathrm{r}}} \sum_{i}^{N_{\boldsymbol{R_\sigma}}} \sum_{j}^{N_{\boldsymbol{R_\sigma+s}}} \frac{q_i^{\mathrm{t}} q_j^{\mathrm{t}}}{\left|\boldsymbol{r}_i^{\boldsymbol{R_\sigma}} - \boldsymbol{r}_j^{\boldsymbol{R_\sigma+s}}\right|} \tag{12}$$

$\boldsymbol{r}_i^{\boldsymbol{R_\sigma}}$ and $\boldsymbol{r}_j^{\boldsymbol{R_\sigma+s}}$ are the distances between the transition charges *i* and *j* on the two chromophores at $\boldsymbol{R_\sigma}$with $N_{\boldsymbol{R_\sigma}}$ atoms and $\boldsymbol{R_\sigma} + \boldsymbol{s}$ with $N_{\boldsymbol{R_\sigma+s}}$ atoms, ε_0 is the vacuum permittivity and ε_{r} is the relative permittivity. Because the Mulliken-decomposed charges densities for *i* and *j* are calculated separately, opposite phases for the transition densities can be obtained for the two chromophores. Using opposite phases in Eq. 12 would lead to the wrong sign for J_{s}. To avoid this problem, for each set of transition charges, we calculated J_{s} for each pair of chromophores in a reference, artificial H-aggregate configuration and identified the correct phase convention to obtain the positive sign for J_{s} that is expected for an H-aggregate. The so verified phase convention, which is equivalent to assuming that the molecular transition dipole moments are pointing in a common direction, was then used to calculate the six excitonic coupling constants to the closest neighboring molecules inside a layer (see Figure 1d). To model the organic absorption spectra, we adjusted ε_{r} manually to recover the positions of the A_1 and H peak of the (AE4T)PbI_4 HOIP and apply the same value to the other perovskites. More advanced methods to treat excitation energy transfer that would overcome difficulties with the phase, such as fragment excitation differences[105,106] or treatment of polarization effects due to surrounding molecules in a TDDFT framework, are available in the community, e.g., in QChem[107]. However, given the computational cost associated with calculating the large HOIP unit cell, the present method presents a good compromise between computational cost and accuracy[104], also in view of the other approximations made in our model.

F. Representation of the Inorganic Exciton Peak

As described in the introduction, in hybrid organic-inorganic materials, the excitons on the organic and inorganic component can couple. However, for 2D HOIPs, the assumption of the weak coupling limit[53] appears to be justified, due to the lack of any discernible splitting in the absorption spectra of any of the (AE4T)PbX_4 (indeed, the organic and inorganic excitons for (AE4T)$PbBr_4$ are almost resonant). Moreover, the observation of nonradiative energy transfer in AE4T-based 2D HOIPs between the two components is consistent with weak coupling[11,31,38,53,83]. Hence, we assume that the interaction of organic and inorganic exciton is negligible for the absorption spectrum. As we show below, the main features in the absorption spectrum can indeed be described without invoking a contribution from coupling between organic and inorganic:

$$I_{\text{total}}(\omega) = I_{\text{org}}(\omega) + I_{\text{inorg}}(\omega). \tag{13}$$

Since the main focus of this paper is on the contribution of the organic component to the experimental absorption spectra, we furthermore model the inorganic exciton contribution to the absorption spectrum fairly simply by a Gaussian line shape function

$$I_{\text{inorg}}(\omega) = I_{\text{inorg,P}} \exp\left(-\frac{\left(\omega - \omega_{\text{inorg}}\right)^2}{2\,\Delta\omega_{\text{inorg}}^2}\right). \tag{14}$$

Here, $I_{\text{inorg,P}}$ is the peak intensity of the inorganic exciton transition, ω_{inorg} is the position of its maximum and $\Delta\omega_{\text{inorg}}$ is its linewidth. The values are extracted from the measured absorption spectra (see Table I). The results discussed below validate the expectation that this simple model for the inorganic exciton peak, combined with the FHH Hamiltonian for the organic part, serves as a sufficient model for the observed exciton spectra. Separate, more predictive phenomenological descriptions of the inorganic excitonic contribution have been demonstrated elsewhere in the literature (see e.g.[51] for a Rydberg model or Ref.[25] and references therein), but are not pursued in this work.

Table I: Parameters used to model the inorganic exciton contribution to the absorption spectra of (AE4T)PbX_4 as a Gaussian line shape function. The parameters were extracted from the experimental absorption spectra from Ref.[31] for (AE4T)$PbCl_4$ and (AE4T)PbI_4 and from Ref.[38] for (AE4T)$PbBr_4$ by

measuring peak position ω_{inorg} and intensity $I_{\mathrm{inorg,P}}$ while adjusting the half-width $\Delta\omega_{\mathrm{inorg}}$ to match the inorganic exciton's peak broadening.

Substance	ω_{inorg} (nm)	$\Delta\omega_{\mathrm{inorg}}$ (nm)	$I_{\mathrm{inorg,P}}$ (a.u.)
(AE4T)$PbCl_4$	327	6	0.556
(AE4T)$PbBr_4$	403	5	0.200
(AE4T)PbI_4	515	10	0.425

Results

Figure 2a shows the absorption spectra of (AE4T)PbX_4 for X = Cl, Br and I. All are characterized by a broad absorption band that originates from the organic framework and resembles the absorption spectrum of the plain (AE4T)·2HX salt films (Figure 2b)[38]. The shoulders in the absorption spectra between 380 nm and 480 nm are attributed to the vibronic progression arising from the coupling of vibrational modes to the electronic transition in the organic components. The narrow peaks in the (AE4T)PbX_4 absorption spectra at 330(2) nm, 404(2) nm and 523(2) nm for X = Cl, Br and I, respectively correspond to the exciton on the inorganic framework[18]. As mentioned above, we work based on the 0th approximation that interactions between the excitons in the organic and inorganic component will not greatly influence the absorption spectra. We focus on modelling the organic contribution to the absorption spectra using the Frenkel-Holstein Hamiltonian, while representing the inorganic contribution by a Gaussian line shape function.

As evident from Figure 2a and b, the absorption spectra corresponding to the organic component in the (AE4T)PbX_4 HOIPs are not identical nor an exact reproduction of the absorption spectra of the (AE4T)·2HX films. Initially, determining trends in the organic contribution to the absorption spectra of the (AE4T)PbX_4 HOIPs is complicated by the presence of the inorganic exciton peak in (AE4T)$PbBr_4$ that obscures the position of the maximum in the organic absorption. Furthermore, for (AE4T)PbI_4, the absorption spectra measured in 1999[38] and 2019[31] peak at different wavelengths, although the shoulders

in the vibronic progression are roughly at the same position. Nonetheless, an overall trend can be observed: As the halide anion varies from I over Br to Cl, the first peak (A_1 peak) and maxima of the organic absorption spectra blue-shift, where the blue-shift for the maxima is slightly stronger than for the A_1 peak. At the same time, the intensities in the vibronic progression decrease from I to Cl (see also Table S1 in the supplementary material). The (AE4T)·2HX films are further blue-shifted and the intensities of the shoulders reduced compared to the 2D HOIPs. Within the (AE4T)·2HX films, the peak of the (AE4T)·2HI is however slightly more red-shifted than those of (AE4T)·2HBr and (AE4T)·2HCl.

The blue-shift can be explained in terms of increasing strength in excitonic coupling within an H-aggregate[65]. In Figure 3, we use the Frenkel-Holstein Hamiltonian to simulate the change in an organic absorption spectrum with increasing strength of excitonic coupling for the four neighbors $J_{\pm 1/2,\pm 1/2}$. For a monomer (black, $J_{\pm 1/2,\pm 1/2} = 0\ \hbar\omega_0$), five peaks are visible, corresponding to the 0-0 (A_1), 0-1 (A_2), 0-2 (A_3), 0-3 (A_4) and 0-4 (A_5) vibrational transitions in the vibronic progression. Here, we chose $\lambda^2 = 1.25$, for which the A_2 peak has a higher intensity than the A_1 peak; for a vibronic progression where $\lambda^2 = 1.0$, the A_1 and A_2 peak would be expected to have the same intensity[65]. Figure 3 shows that when increasing the strength of the excitonic coupling $J_{\pm 1/2,\pm 1/2}$, the intensity of the A_1 band diminishes, while the maximum of the absorption band moves from the A_2 peak (black and dark blue lines) to first the A_3 peak (blue and purple lines), then the A_4 peak (pink and orange lines) and finally A_5 peak (yellow line). Based on this picture, we expect the excitonic coupling of the Frenkel exciton on the organic component to diminish from the (AE4T)·2HX films to (AE4T)$PbCl_4$ and to be lowest for the (AE4T)PbI_4 HOIP.

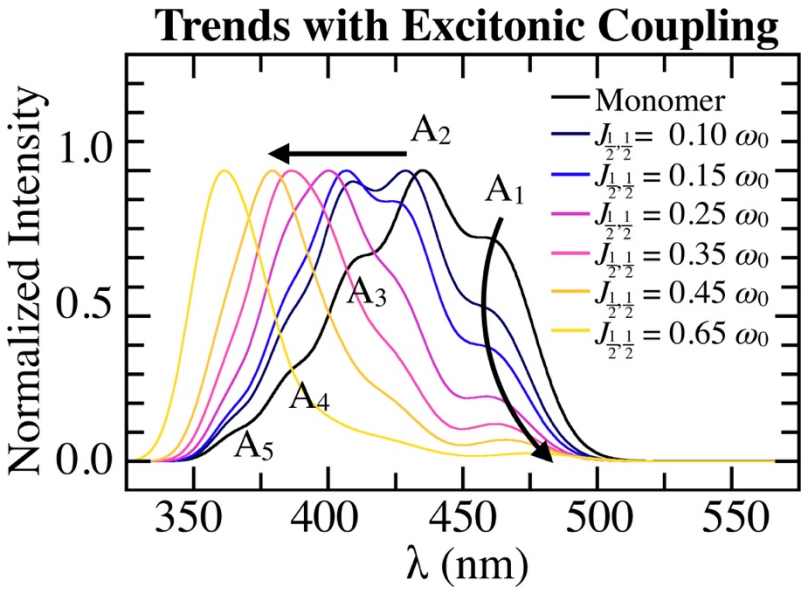

Figure 3: Evolution of the absorption spectrum simulated with the Frenkel-Holstein Hamiltonian for increasing exciton coupling strength, varying from $J_{\pm 1/2,\pm 1/2} = 0.0\ \hbar\omega_0$ (monomer, black) to $J_{\pm 1/2,\pm 1/2} = 0.65\ \hbar\omega_0$ (yellow) for the transition from the electronic ground state to the electronically first excited state. The excitonic couplings are given in units of vibrational energy ($\hbar\omega_0$ = 1440 cm^{-1}, 0.18 eV). For the monomer, labelling according to the vibrational transition is again supplied where A_1 corresponds to the transition from the ground state to the vibrational ground state of the first electronically excited state. For the simulations, N_h = 36 molecules were taken with a maximum of 4 vibrational quanta. In addition, $\omega_{0-0} + D$ was set to 464 nm.

In order to substantiate this expectation, we obtained organic absorption spectra for different four neighbor couplings $J_{\pm 1/2,\pm 1/2}$ with the Frenkel-Holstein Hamiltonian and fit them to the experimental absorption spectra. As described in the methods section, we also add a Gaussian peak to the organic absorption spectra obtained with the Frenkel-Holstein Hamiltonian to model the contribution of the inorganic exciton, and use the Pendry R-factor R_P to evaluate the agreement between fitted and experimental spectra. The Pendry R-factor is a measure for the agreement between two continuous curves, with particular sensitivity towards peak positions. It can range between 0 (perfect correlation) and 2 (anticorrelation), where a value of R_P = 1 would describe uncorrelated data[96]. Table II shows that we obtain reasonable values for R_P, especially considering the low number of parameters employed. Figure 4 shows that the fitted absorption spectra of the organic component are overall narrower than

the experimental ones, which can be attributed to the fact that we model only the first electronic transition and do not include any further broadenings due to thermal fluctuations or lattice disorder. The slightly higher value of the Pendry R-factor for (AE4T)$PbBr_4$ is most likely a combined result of capturing the shape of the inorganic exciton peak less well than for X = Cl and X = I, the disagreement in the spectral broadening between the simulated and experimental absorption spectra as well as other possible model limitations on the high-energy side of the organic-derived features. In the supplementary material Tables S2 and S3 and Figure S4, we show that the fitting results are not much influenced by the choice of system-independent modeling parameters like the number of chromophores N_h, the number of neighbors, the broadening of the organic absorption (Eq. (9)) or by replacing the Pendry R-factor by a root-mean-square error to evaluate the goodness of the fit. We also show that the fitting results for the organic absorption spectra do not depend strongly on the choice of treatment for the inorganic exciton peak.

Table II: Excitonic coupling constants obtained by fitting the Frenkel-Holstein Hamiltonian absorption spectrum calculated for four-nearest-neighbor interactions $J_{\pm 1/2,\pm 1/2}$ for the (AE4T)·2HX films and the (AE4T)PbX_4 HOIPs. The excitonic couplings are given in units of vibrational energy ($\hbar\omega_0$=1440 cm^{-1}, 0.18 eV). For the fit of the organic absorption spectra, the following spectral ranges were considered: 315 nm -- 520 nm for X = Cl, 295 nm -- 520 nm for X = Br and 330 nm to 550 nm for X = I for (AE4T)PbX_4 and for (AE4T)·2HX 300 – 520 nm. The Pendry R-factor is given for the divergence in intensities between the experimental and theoretical spectrum when both experimental and theoretical spectra are normalized to the peak of the organic absorption spectrum.

Substance	$J_{\pm 1/2,\pm 1/2}(\hbar\omega_0)$	Pendry R-factor
(AE4T)$PbCl_4$	0.36	0.168
(AE4T)$PbBr_4$	0.31	0.219
(AE4T)PbI_4	0.23	0.166

(AE4T)·2HCl	0.55	0.240
(AE4T)·2HBr	0.55	0.165
(AE4T)·2HI	0.36	0.246

The fitted absorption spectra in Figure 4 are in overall good agreement with the experimental absorption spectra. For all spectra, the positions of the peaks in the vibronic progression of the organic absorption spectra are reproduced. For the systems (AE4T)$PbCl_4$ (a), the (AE4T)·2HX films (b, d, e), and (AE4T)PbI_4 (e), the fitted spectrum captures the experimental spectrum's maximum (see also Table S1 in the supplementary material). For (AE4T)$PbBr_4$ (Figure 4 c), the presence of the inorganic excitonic peak prohibits identification of the organic band's maximum, however, the fitted spectrum reproduces the shape of the experimental spectrum well. For (AE4T)PbI_4, the maximum of the spectrum measured in 2019[31] is well recovered while the maximum of the spectrum measured in 1999[38] corresponds to a shoulder of much lower intensity. The mismatch of the intensities to the spectrum from 1999 is in so far only a smaller deviation, because the shoulders in the simulated absorption spectrum are at roughly the same wavelengths as the shoulders in both experimental spectra. From Figure 3, it can be seen that if the excitonic coupling for the spectrum from 1999 were higher than for the spectrum from 2019, then shoulders in the vibronic progression should also be more blue-shifted which does not appear to be the case.

In Figure 4 g and h, the fitted organic absorption spectra without the inorganic exciton peak are shown together, providing a direct visual comparison. The fitted organic absorption spectra recover the trends observed for the organic band in the experimental absorption spectra (Figure 2). As in the experiment, the vibronic features have the highest intensity for (AE4T)PbI_4 (Figure 4 e) and diminish towards X = Cl and the (AE4T)·2HX films. Table II shows that, in agreement with our qualitative assessment above, this decrease in the intensity is due to an increase in the excitonic coupling in going from (AE4T)PbI_4 to (AE4T)$PbCl_4$ films. Similarly, the shift of the maximum from X = Cl and X = Br to X = I in the (AE4T)PbX_4 HOIPs can now be rationalized in terms of the vibronic progression (Figure 4 g): for X =

I, the A_3 peak of the vibronic progression forms the maximum of the H-band, while for X = Cl and Br, the excitonic coupling is strong enough to turn the A_4 peak into the overall maximum. As already observed for the experimental absorption spectra, the (AE4T)·2HI film shows a weaker coupling than (AE4T)·2HBr and (AE4T)·2HCl film, probably due to a change in accommodation of the halide anion.

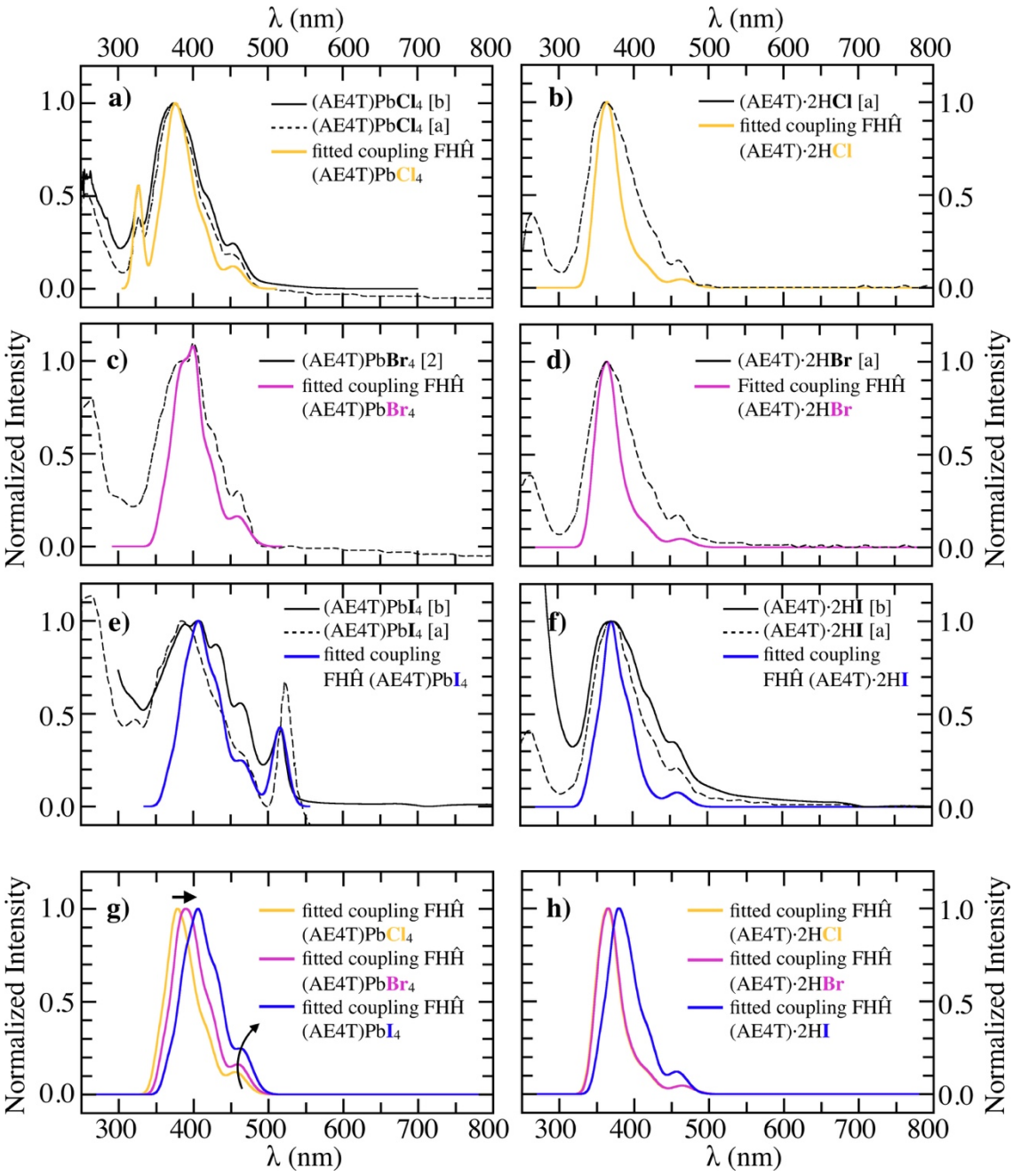

Figure 4: Comparison between experimental UV-vis absorption spectra (black) adapted with permission from Ref.[38]. Copyright 1999 American Chemical Society (marked as [a]), and adapted from

Ref.[31] with permission from the Royal Society of Chemistry (marked as [b]), and fitted absorption spectra utilizing on the four interactions $J_{\pm 1/2,\pm 1/2}$. a) (AE4T)$PbCl_4$ absorption spectrum fitted (yellow) to UV-vis from Ref.[31] (black solid), Ref.[38] (black dashed) shown for reference b) (AE4T)·2HCl absorption spectrum fitted (yellow) to UV-vis from Ref.[38] (black solid) c) (AE4T)$PbBr_4$ absorption spectrum fitted (purple) to UV-vis from Ref.[38] (black solid) d) (AE4T)·2HBr absorption spectrum fitted (purple) to UV-vis from Ref.[38] (black solid) e) (AE4T)PbI_4 absorption spectrum fitted (blue) to UV-vis from Ref.[31] (black solid), Ref.[38] (black dashed) shown for reference, f) (AE4T)·2HCl absorption spectrum fitted (blue) to UV-vis from Ref.[31] (black solid), Ref.[38] (black dashed) shown for reference. g) For better comparison, the organic parts of the absorption spectra for fits of (AE4T)$PbCl_4$ (yellow), (AE4T)$PbBr_4$ (purple) and (AE4T)PbI_4 (yellow) are shown h) comparison between fits for (AE4T)·2HCl (yellow), (AE4T)·2HBr (purple) and (AE4T)·2HI (yellow).

Finally, we briefly consider the model of the inorganic exciton peaks by a Gaussian line shape function. This approach reproduces the overall shape of the organic exciton to a good approximation. Interestingly, Table I shows that the optimal parameters to represent the shape of the inorganic exciton peak differ between the three HOIPs, e.g. in width of the excitonic peak. These differences could either arise due to differences in film quality between the perovskites or be related to the properties of the inorganic exciton, effects that are beyond the scope of the present work.

While the overall position of the shoulders and peaks in the organic experimental absorption spectrum are well captured by the fit, it is well established that for molecular assemblies and 2D aggregates that extended neighbor couplings cannot be neglected and grow in importance with molecular length[52,108]. In order to include the effect of extended neighbor couplings and, more importantly, to see how the strength of the excitonic coupling can be related to structural parameters in the HOIP, we calculate the excitonic coupling based on the underlying geometry of the organic layer in the HOIPs. For this, we use atomic structures from DFT-PBE+TS structure relaxation[30,31]. As described in the methods section, we calculate transition densities for a single chromophore using LR-TDDFT and then use Eq. (5) to calculate the Coulombic exciton couplings between the chromophores inside the organic layers based on the DFT-PBE+TS geometries for up to 6th neighbor couplings. Given the good agreement of the

DFT-PBE+TS lattice vectors with the experimental lattice vectors[30] and the lack of an excitonic peak in the organic absorption band, we use the experimental absorption spectrum from 2019 of (AE4T)PbI_4 to adjust the dielectric constant so that the calculated absorption spectrum reproduces the position of the A_1 peak and the maximum of the organic absorption band. We find $\varepsilon_r = 2.8$, which is slightly lower than the dielectric constant of $\varepsilon_r = 3.5$ measured for quaterthiophene[109]. We apply the same dielectric constant for all three HOIPs and again model the contribution of the inorganic peak to the spectra by a Gaussian line shape function. In Table III, the excitonic couplings with the first to sixth nearest neighbors are listed. Compared to the fit, the individual excitonic couplings are expectedly smaller as the excitonic coupling is divided onto a larger set of neighbors. The trend between the fitted $J_{\pm 1/2,\pm 1/2}$ values and the leading LR-TDDFT based extended excitonic couplings is similar in that all of them decrease as the halide X progresses from Cl to Br to I. However, the ratios between J values for different compounds differ in detail when comparing the fitted $J_{\pm 1/2,\pm 1/2}$ values and the LR-TDDFT J values, reflecting the fact that the fits, qualitatively speaking, "wrap" the behavior of different longer-ranged couplings (Table III and Figure S5) into a few leading fitted couplings.

Figure 5 a--c show the comparison of the experimental and the calculated absorption spectra based on the geometry-based excitonic couplings. The overall shape and reproduction of the intensities in the vibronic progression of the organic absorption band is improved compared to the results from the fit using only the four excitonic couplings $J_{\pm 1/2,\pm 1/2}$ in Figure 4. Interestingly, for (AE4T)$PbBr_4$, the maximum in the absorption spectrum shifts from A_4 to A_3 in the computational model compared to the fitted model (see Figure 4b and d vs. Figure 3c and g). This means that the intensity of the inorganic exciton peak $I_{\mathrm{inorg,P}}$ (Table I) has to be reduced to 0.08.

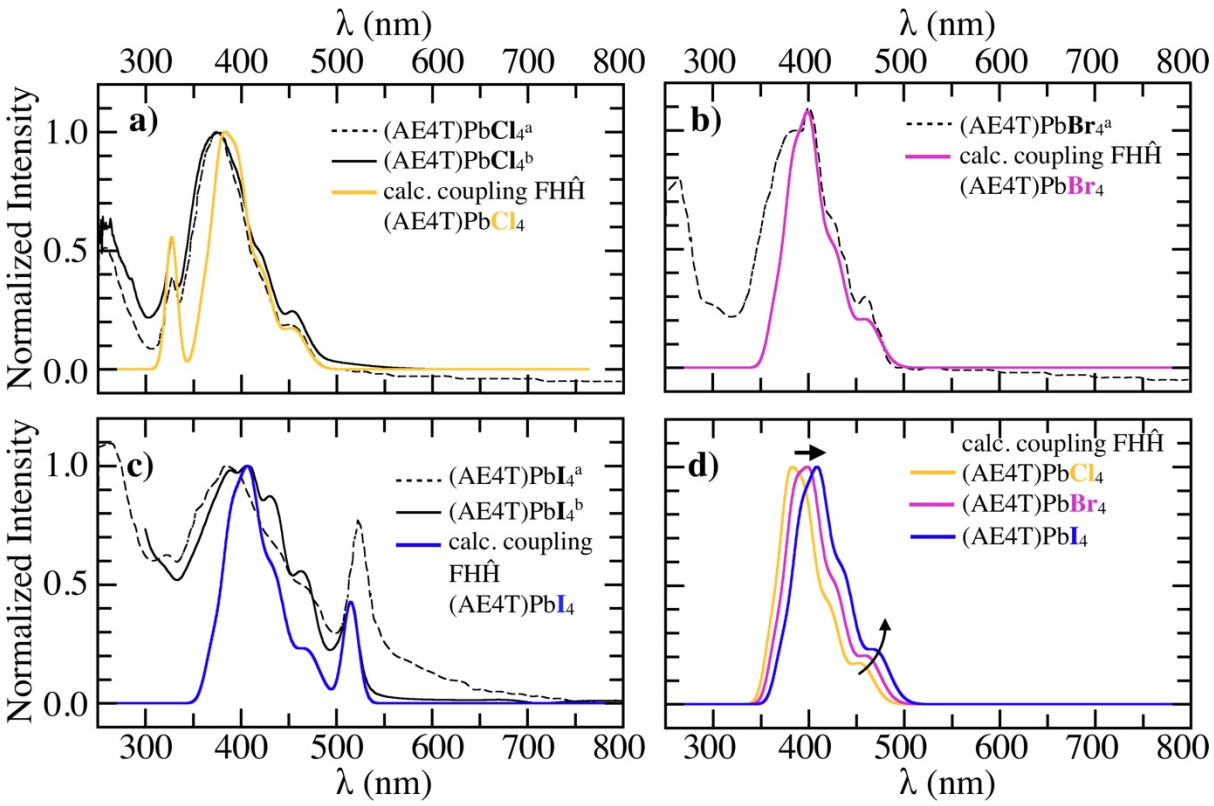

Figure 5: Comparison between experimental UV-vis absorption spectra (black) adapted with permission from Ref.[38]. Copyright 1999 American Chemical Society (marked as [a]), and adapted from Ref.[31] with permission from the Royal Society of Chemistry (marked as [b]), and calculated a) $(AE4T)PbCl_4$ (yellow), b) $(AE4T)PbBr_4$ (purple) c) $(AE4T)PbI_4$ (blue) spectra based on LR-TDDFT evaluation of the extended couplings. The transition energy of the A_1 band was taken from the above fitted spectra. d) shows the comparison of the calculated spectra for $(AE4T)PbCl_4$ (yellow), $(AE4T)PbBr_4$ (purple) and $(AE4T)PbI_4$ (blue).

For $(AE4T)PbBr_4$ (Figure 5b) and $(AE4T)PbI_4$ (5c), the positions of the peaks and shoulders in the vibronic progression of the organic contribution to the experimental absorption spectra are well described while the intensities of the vibronic progression are exceedingly well reproduced for $(AE4T)PbBr_4$ and less well for $(AE4T)PbI_4$. For $(AE4T)PbCl_4$ (5a), while the intensities in the vibronic progression are very well captured, the simulated absorption spectrum peaks at higher wavelengths than the experimental absorption spectrum. Figure S6 in the supplementary material shows that the dielectric

constant for the Cl-based perovskites needs to be reduced from $\varepsilon = 2.8$ to $\varepsilon = 2.2$ in order to increase the excitonic coupling strengths enough to reproduce the position of the main peak in experimental spectrum. The increase would however come at the cost of a worse agreement in the intensities. In principle, a change of the dielectric constant could be physically justified given the increase in band gap of the inorganic from I to Cl[38]. Given that Dunlap-Shohl *et al.*[31] observe that the ***a***-lattice parameter is underestimated by the theoretical structure (other lattice parameters are not known experimentally to our knowledge), it may also be that the DFT-PBE+TS structure for (AE4T)$PbCl_4$ does not exactly reproduce the structure assumed in room-temperature experiments.

Overall, Figure 5d shows that the trends in the absorption spectra of a blue-shift from (AE4T)PbI_4 to (AE4T)$PbCl_4$ accompanied by a decrease in the intensities of the A_1 and A_2 shoulders are captured. Table III shows that this is caused by an increase in excitonic coupling, which at the same time correlates with decrease of the area per molecule. This correlation is not unexpected: the smaller the area per molecule, the closer the molecules are packed and hence, the excitonic coupling increases according to Eq. (11). The change in packing density is due to a templating effect from the inorganic framework, a well-known occurrence in HOIPs[10]. The size of the unit cell increases from Cl to I due to the increase in Pb-X bond length. While the Pb-Cl bond length is on average 2.93 Å in the present structural model, the Pb-Br bond length averages to 3.00 Å and the Pb-I bond length to 3.18 Å, increasing the space that the molecules have to fill and thus reducing the excitonic coupling from Cl to I. The molecules adapt to the increase in space by increasing the tilt angle to the surface normal from Cl to I (θ_{Cl} = 55°, θ_{Br} = 57°, θ_I = 60°, see Figure 1) and by diminishing the herringbone angle σ between the molecules (σ_{Cl} = 50°, σ_{Br} = 47°, σ_I = 41°). It is likely due to this change in molecular geometry that the excitonic couplings of e.g. (AE4T)$PbCl_4$ cannot be simply scaled to obtain the excitonic couplings of X = Br and I (see Figure S5 in the supplementary material).

The stronger excitonic coupling found in the fit for the (AE4T)·2HX films hence suggests that the films are more densely packed than the organic molecules in the HOIPs. This would be in line with the experimentally determined lattice parameters for quaterthiophene (OT4) that show a much smaller area per molecule (see Table III).

Table III*:* For the (AE4T)PbX_4 HOIPs, the in-organic plane lattice parameters and area per molecule, both extracted from DFT-PBE+TS calculations[30,31], as well as the excitonic couplings between the six nearest neighboring molecules from LR-TDDFT transition density calculations are listed. The excitonic couplings are given in units of vibrational energy ($\hbar\omega_0$ = 1440 cm^{-1}, 0.18 eV). For comparison, the experimental lattice parameters of the low-temperature polymorph (LT) of quaterthiophene (OT4)[79] are shown. ***b*** and ***c*** refer to the lattice vectors of the 2D HOIP and should not be confused with the lattice vectors used for the FHH simulations ($\boldsymbol{c}' = \boldsymbol{c}$ and $\boldsymbol{b}' = \frac{1}{2}\boldsymbol{b}$).

Substance	Lattice Parameters		Area/molecule	Calculated Excitonic Couplings					
	b (Å)	***c*** (Å)	(Å^2)	$J_{1,0}$ ($\hbar\omega_0$)	$J_{\frac{1}{2}\frac{1}{2}}$ ($\hbar\omega_0$)	$J_{\frac{3}{2}\frac{1}{2}}$ ($\hbar\omega_0$)	$J_{0,1}$ ($\hbar\omega_0$)	$J_{2,0}$ ($\hbar\omega_0$)	$J_{1,1}$ ($\hbar\omega_0$)
(AE4T)$PbCl_4$	11.30[31]	10.95[31]	30.93	0.186	0.128	0.060	0.012	0.054	0.014
(AE4T)$PbBr_4$	11.60[30]	11.48[30]	33.29	0.180	0.115	0.054	0.001	0.051	0.008
(AE4T)PbI_4	12.10[30]	12.23[30]	37.00	0.170	0.099	0.046	0.012	0.046	0.004
LT-OT4	6.085(2)[79]	7.858(2)[79]	23.91						

Conclusion

In conclusion, we demonstrate that the Frenkel-Holstein Hamiltonian can be applied to simulate and explain the vibronic progression in the absorption spectrum of the organic component in the 2D hybrid organic-inorganic perovskites (AE4T)PbX_4 (X = Cl, Br, I). Based on both fits to the absorption spectra and LR-TDDFT calculations of the chromophore in combination with the DFT-PBE+TS calculated atomic structure of the organic layers, we derived excitonic couplings between the organic molecules that reproduce the trends in vibronic progression of the experimental absorption spectra.

We find that the choice of the halide anion in the inorganic component templates the strength of the excitonic coupling between the molecules in the organic component with large excitonic couplings for X = Cl and small coupling strengths for I. We can relate coupling strengths to the varying space occupied by a given molecule where molecules are more confined for X = Cl than for X = I. The choice of the halide anion in this manner influences the shape of the vibronic progression in the organic absorption spectrum. As a result, the simulation of the absorption spectrum is sensitive to the underlying structural model.

In future work, we intend to include the contribution of the inorganic exciton directly into the Frenkel Holstein-Hamiltonian to investigate exciton-exciton coupling between the organic and inorganic framework in the optical spectra. Additionally, we plan to combine our model directly with *ab initio* calculations to predict experimental absorption and emission spectra.

Supplementary Material

See supplementary material for coupling between organic layers at the example of (AE4T)$PbBr_4$, convergence of the simulated absorption with number of monomers and vibrational quanta, the extraction of the Huang-Rhys factor from the OT4 emission spectrum, the comparison of peak positions in the experimental and simulated absorption spectra; fitting results without and under subtraction of a Gaussian peak from the experimental absorption spectra, dependence of the fit on different choices for Gaussian broadening, number of monomers in the simulation, evaluation of fitting result and number of neighbors; excitonic couplings between organic chromophores as a function of position/distance; and different choice for ε_r for (AE4T)$PbCl_4$.

Acknowledgement

This work was carried out with the financial support from the National Science Foundation (F.C.S., DMR-1810838 and V.B., DMR-1729297). S.M.J. thanks the Deutsche Forschungsgemeinschaft (DFG, German Research Foundation) for a postdoctoral fellowship, grant number 393196393. We thank David Bialas for valuable discussions and for help with the calculation of the LR-TDDFT-based excitonic couplings and April Oleson for her help with the calculation of the OT4 emission spectrum. We thank David B. Mitzi, Manoj K. Jana and Wiley Dunlap-Shohl for supplying the adsorption data for (AE4T)·2HI from Ref.[31]. V.B. and S.M.J thank David B. Mitzi and Kenan Gundogdu for useful discussions.

References

[1] W.S. Yang, B.W. Park, E.H. Jung, N.J. Jeon, Y.C. Kim, D.U. Lee, S.S. Shin, J. Seo, E.K. Kim, J.H. Noh, and S. Il Seok, Science (80-.). **356**, 1376 (2017).

[2] W.J. Yin, T. Shi, and Y. Yan, Adv. Mater. **26**, 4653 (2014).

[3] A. Kojima, K. Teshima, Y. Shirai, and T. Miyasaka, J. Am. Chem. Soc. **131**, 6050 (2009).

[4] I. Chung, B. Lee, J. He, R.P.H. Chang, and M.G. Kanatzidis, Nature **485**, 486 (2012).

[5] H.-S. Kim, C.-R. Lee, J.-H. Im, K.-B. Lee, T. Moehl, A. Marchioro, S.-J. Moon, R. Humphry-Baker, J.-H. Yum, J.E. Moser, M. Grätzel, and N.-G. Park, Sci. Rep. **2**, 591 (2012).

[6] M.M. Lee, J. Teuscher, T. Miyasaka, T.N. Murakami, and H.J. Snaith, Science (80-.). **338**, 643 (2012).

[7] NREL, Best Res. Effic. Chart (2019).

[8] M.B. Johnston and L.M. Herz, Acc. Chem. Res. **49**, 146 (2016).

[9] K. Wang, D. Yang, C. Wu, M. Sanghadasa, and S. Priya, Prog. Mater. Sci. **106**, 100580 (2019).

[10] M.D. Smith, B.A. Connor, and H.I. Karunadasa, Chem. Rev. **119**, 3104 (2019).

[11] K. Chondroudis and D.B. Mitzi, Chem. Mater. **11**, 3028 (1999).

[12] X. Hong, T. Ishihara, and A. V. Nurmikko, Solid State Commun. **84**, 657 (1992).

[13] M. Era, S. Morimoto, T. Tsutsui, and S. Saito, Appl. Phys. Lett. **65**, 676 (1994).

[14] T. Hattori, T. Taira, M. Era, T. Tsutsui, and S. Saito, Chem. Phys. Lett. **254**, 103 (1996).

[15] D. Liang, Y. Peng, Y. Fu, M.J. Shearer, J. Zhang, J. Zhai, Y. Zhang, R.J. Hamers, T.L. Andrew, and S. Jin, ACS Nano **10**, 6897 (2016).

[16] M. Yuan, L.N. Quan, R. Comin, G. Walters, R. Sabatini, O. Voznyy, S. Hoogland, Y. Zhao, E.M. Beauregard, P. Kanjanaboos, Z. Lu, D.H. Kim, and E.H. Sargent, Nat. Nanotechnol. **11**, 872 (2016).

[17] J. Byun, H. Cho, C. Wolf, M. Jang, A. Sadhanala, R.H. Friend, H. Yang, and T.-W. Lee, Adv. Mater. **28**, 7515 (2016).

[18] N. Wang, L. Cheng, R. Ge, S. Zhang, Y. Miao, W. Zou, C. Yi, Y. Sun, Y. Cao, R. Yang, Y. Wei, Q. Guo, Y. Ke, M. Yu, Y. Jin, Y. Liu, Q. Ding, D. Di, L. Yang, G. Xing, H. Tian, C. Jin, F. Gao, R.H. Friend, J. Wang, and W. Huang, Nat. Photonics **10**, 699 (2016).

[19] Y. Kim, H. Cho, and T. Lee, Proc. Natl. Acad. Sci. **113**, 11694 (2016).

[20] G. Long, C. Jiang, R. Sabatini, Z. Yang, M. Wei, L.N. Quan, Q. Liang, A. Rasmita, M. Askerka, G.

Walters, X. Gong, J. Xing, X. Wen, R. Quintero-Bermudez, H. Yuan, G. Xing, X.R. Wang, D. Song, O. Voznyy, M. Zhang, S. Hoogland, W. Gao, Q. Xiong, and E.H. Sargent, Nat. Photonics **12**, 528 (2018).

[21] Y. Dong, Y. Zhang, X. Li, Y. Feng, H. Zhang, and J. Xu, Small **15**, 1970209 (2019).

[22] J. Wang, C. Zhang, H. Liu, R. McLaughlin, Y. Zhai, S.R. Vardeny, X. Liu, S. McGill, D. Semenov, H. Guo, R. Tsuchikawa, V. V. Deshpande, D. Sun, and Z.V. Vardeny, Nat. Commun. **10**, 1 (2019).

[23] L. Mao, C.C. Stoumpos, and M.G. Kanatzidis, J. Am. Chem. Soc. **141**, 1171 (2019).

[24] B. Saparov and D.B. Mitzi, Chem. Rev. **116**, 4558 (2016).

[25] C. Katan, N. Mercier, and J. Even, Chem. Rev. **119**, 3140 (2019).

[26] Y.Y. Li, C.K. Lin, G.L. Zheng, Z.Y. Cheng, H. You, W.D. Wang, and J. Lin, Chem. Mater. **18**, 3463 (2006).

[27] M.K. Jana, S.M. Janke, D.J. Dirkes, S. Dovletgeldi, C. Liu, X. Qin, K. Gundogdu, W. You, V. Blum, and D.B. Mitzi, J. Am. Chem. Soc. **141**, 7955 (2019).

[28] M.K. Jana, C. Liu, S. Lidin, D.J. Dirkes, W. You, V. Blum, and D.B. Mitzi, Chem. Mater. **0**, acs. chemmater.9b03208 (2019).

[29] B. Traore, L. Pedesseau, L. Assam, X. Che, J.C. Blancon, H. Tsai, W. Nie, C.C. Stoumpos, M.G. Kanatzidis, S. Tretiak, A.D. Mohite, J. Even, M. Kepenekian, and C. Katan, ACS Nano **12**, 3321 (2018).

[30] C. Liu, W. Huhn, K.-Z. Du, A. Vazquez-Mayagoitia, D. Dirkes, W. You, Y. Kanai, D.B. Mitzi, and V. Blum, Phys. Rev. Lett. **121**, 146401 (2018).

[31] W. Dunlap-Shohl, E.T. Barraza, A. Barrette, S. Dovletgeldi, G. Findik, D. Dirkes, C. Liu, M.K. Jana, V. Blum, W. You, K. Gundogdu, A. Stiff-Roberts, and D.B. Mitzi, Mater. Horizons (2019).

[32] M. Braun, W. Tuffentsammer, H. Wachtel, and H.C. Wolf, Chem. Phys. Lett. **307**, 373 (1999).

[33] M. Braun, W. Tuffentsammer, H. Wachtel, and H.C. Wolf, Chem. Phys. Lett. **303**, 157 (1999).

[34] K. Ema, M. Inomata, Y. Kato, H. Kunugita, and M. Era, Phys. Rev. Lett. **100**, 257401 (2008).

[35] M. Era, K. Maeda, and T. Tsutsui, Chem. Phys. Lett. **296**, 417 (1998).

[36] K. Nagao, N. Kawano, M. Koshimizu, and K. Asai, Jpn. J. Appl. Phys. **53**, 02BC21 (2014).

[37] N. Kawano, M. Koshimizu, and K. Asai, J. Phys. Chem. C **116**, 22992 (2012).

[38] D.B. Mitzi, K. Chondroudis, and C.R. Kagan, Inorg. Chem. **38**, 6246 (1999).

[39] X. Blase, I. Duchemin, and D. Jacquemin, Chem. Soc. Rev. **47**, 1022 (2018).

[40] S. Refaely-Abramson, R. Baer, and L. Kronik, Phys. Rev. B - Condens. Matter Mater. Phys. **84**, 22 (2011).

[41] T. Körzdörfer and J.L. Brédas, Acc. Chem. Res. **47**, 3284 (2014).

[42] G. Giorgi, K. Yamashita, and M. Palummo, J. Phys. Chem. Lett. **9**, 5891 (2018).

[43] A. Molina-Sánchez, ACS Appl. Energy Mater. **1**, 6361 (2018).

[44] J.-C. Blancon, A. V. Stier, H. Tsai, W. Nie, C.C. Stoumpos, B. Traoré, L. Pedesseau, M. Kepenekian, F. Katsutani, G.T. Noe, J. Kono, S. Tretiak, S.A. Crooker, C. Katan, M.G. Kanatzidis, J.J. Crochet, J. Even, and A.D. Mohite, Nat. Commun. **9**, 2254 (2018).

[45] J. Yin, H. Li, D. Cortecchia, C. Soci, and J.L. Brédas, ACS Energy Lett. **2**, 417 (2017).

[46] C. Quarti, N. Marchal, and D. Beljonne, J. Phys. Chem. Lett. **9**, 3416 (2018).

[47] Y. Cho and T.C. Berkelbach, J. Phys. Chem. Lett. **10**, 6189 (2019).

[48] S.F. Zhang, X.K. Chen, A.M. Ren, H. Li, and J.L. Bredas, ACS Energy Lett. **4**, 17 (2019).

[49] Z. Zhang, W.H. Fang, M. V. Tokina, R. Long, and O. V. Prezhdo, Nano Lett. **18**, 2459 (2018).

[50] J. Leveillee, C. Katan, L. Zhou, A.D. Mohite, J. Even, S. Tretiak, A. Schleife, and A.J. Neukirch, Phys. Rev. Mater. **2**, 105406 (2018).

[51] M.D. Smith, L. Pedesseau, M. Kepenekian, I.C. Smith, C. Katan, J. Even, and H.I. Karunadasa, Chem. Sci. **8**, 1960 (2017).

[52] N.J. Hestand and F.C. Spano, Chem. Rev. **118**, 7069 (2018).

[53] V.M. Agranovich, Y.N. Gartstein, and M. Litinskaya, Chem. Rev. **111**, 5179 (2011).

[54] J. Even, S. Boyer-Richard, M. Carignano, L. Pedesseau, J.-M. Jancu, and C. Katan, in *Phys. Simul. Optoelectron. Devices XXIV*, edited by B. Witzigmann, M. Osiński, and Y. Arakawa (2016), p. 97421A.

[55] E. Rabani, R. Baer, and D. Neuhauser, Phys. Rev. B **91**, 235302 (2015).

[56] P. Umari, E. Mosconi, and F. De Angelis, J. Phys. Chem. Lett. **9**, 620 (2018).

[57] E.G. McRae and M. Kasha, J. Chem. Phys. **28**, 721 (1958).

[58] M. Kasha, Radiat. Res. **20**, 55 (1963).

[59] M. Kasha, H.R. Rawls, and M. Ashraf El-Bayoumi, Pure Appl. Chem. **11**, 371 (1965).

[60] R.L. Fulton and M. Gouterman, J. Chem. Phys. **35**, 1059 (1961).

[61] A. Witkowski and W. Moffitt, J. Chem. Phys. **33**, 872 (1960).

[62] R.E. Merrifield, Radiat. Res. **20**, 154 (1963).

[63] R.E. Merrifield, J. Chem. Phys. **40**, 445 (1964).

[64] T. Holstein, Ann. Phys. (N. Y). **8**, 325 (1959).

[65] F.C. Spano, Acc. Chem. Res. **43**, 429 (2010).

[66] H. Yamagata, J. Norton, E. Hontz, Y. Olivier, D. Beljonne, J.L. Brédas, R.J. Silbey, and F.C. Spano, J. Chem. Phys. **134**, 204703 (2011).

[67] N.J. Hestand, H. Yamagata, B. Xu, D. Sun, Y. Zhong, A.R. Harutyunyan, G. Chen, H.-L. Dai, Y. Rao, and F.C. Spano, J. Phys. Chem. C **119**, 22137 (2015).

[68] S.-H. Lim, T.G. Bjorklund, F.C. Spano, and C.J. Bardeen, Phys. Rev. Lett. **92**, 107402 (2004).

[69] F.C. Spano, J. Chem. Phys. **120**, 7643 (2004).

[70] F.C. Spano, Annu. Rev. Phys. Chem. **57**, 217 (2006).

[71] F.C. Spano, Phys. Rev. B **71**, 235208 (2005).

[72] Z. Zhao and F.C. Spano, J. Chem. Phys. **122**, 114701 (2005).

[73] F.C. Spano, L. Silvestri, P. Spearman, L. Raimondo, and S. Tavazzi, J. Chem. Phys. **127**, 184703 (2007).

[74] L. Silvestri, S. Tavazzi, P. Spearman, L. Raimondo, and F.C. Spano, J. Chem. Phys. **130**, 234701 (2009).

[75] A. Stradomska and P. Petelenz, J. Chem. Phys. **131**, 044507 (2009).

[76] A. Stradomska and P. Petelenz, J. Chem. Phys. **130**, 094705 (2009).

[77] K.Z. Du, Q. Tu, X. Zhang, Q. Han, J. Liu, S. Zauscher, and D.B. Mitzi, Inorg. Chem. **56**, 9291 (2017).

[78] C.C. Mattheus, G.A. de Wijs, R.A. de Groot, and T.T.M. Palstra, J. Am. Chem. Soc. **125**, 6323 (2003).

[79] T. Siegrist, C. Kloc, R.A. Laudise, H.E. Katz, and R.C. Haddon, Adv. Mater. **10**, 379 (1998).

[80] L. Antolini, G. Horowitz, F. Kouki, and F. Garnier, Adv. Mater. **10**, 382 (1998).

[81] D.B. Mitzi, Inorg. Chem. **39**, 6107 (2000).

[82] X.-H. Zhu, N. Mercier, P. Frère, P. Blanchard, J. Roncali, M. Allain, C. Pasquier, and A. Riou, Inorg. Chem. **42**, 5330 (2003).

[83] D.B. Mitzi, K. Chondroudis, and C.R. Kagan, IBM J. Res. Dev. **45**, 29 (2001).

[84] B.M. and T.W. et al Mark Mitchell, Http//Markummitchell.Github.Io/Engauge-Digitizer, Last

Accessed July 11, 2019 (n.d.).

[85]Https://Materials.Hybrid3.Duke.Edu (2019).

[86] J.P. Perdew, K. Burke, and M. Ernzerhof, Phys. Rev. Lett. **77**, 3865 (1996).

[87] A. Tkatchenko and M. Scheffler, Phys. Rev. Lett. **102**, 073005 (2009).

[88] V. Blum, R. Gehrke, F. Hanke, P. Havu, V. Havu, X. Ren, K. Reuter, and M. Scheffler, Comput. Phys. Commun. **180**, 2175 (2009).

[89] M.R. Philpott, J. Chem. Phys. **55**, 2039 (1971).

[90] F.C. Spano, J. Chem. Phys. **116**, 5877 (2002).

[91] W. Gebauer, M. Sokolowski, and E. Umbach, Chem. Phys. **227**, 33 (1998).

[92] R.S. Becker, J. Seixas de Melo, A.L. Maçanita, and F. Elisei, J. Phys. Chem. **100**, 18683 (1996).

[93] M. Laicini, P. Spearman, S. Tavazzi, and A. Borghesi, Phys. Rev. B **71**, 045212 (2005).

[94] J.B. Pendry, J. Phys. C Solid State Phys. **13**, 937 (1980).

[95] V. Blum and K. Heinz, Comput. Phys. Commun. **134**, 392 (2001).

[96] C. Baldauf and M. Rossi, J. Phys. Condens. Matter **27**, 493002 (2015).

[97] F. Schubert, M. Rossi, C. Baldauf, K. Pagel, S. Warnke, G. Von Helden, F. Filsinger, P. Kupser, G. Meijer, M. Salwiczek, B. Koksch, M. Scheffler, and V. Blum, Phys. Chem. Chem. Phys. **17**, 7373 (2015).

[98] D. Beljonne, J. Cornil, R. Silbey, P. Millié, and J.L. Brédas, J. Chem. Phys. **112**, 4749 (2000).

[99] K.A. Kistler, F.C. Spano, and S. Matsika, J. Phys. Chem. B **117**, 2032 (2013).

[100] J.-D. Chai and M. Head-Gordon, J. Chem. Phys. **128**, 084106 (2008).

[101] F. Weigend and R. Ahlrichs, Phys. Chem. Chem. Phys. **7**, 3297 (2005).

[102] B. Bouvier, T. Gustavsson, D. Markovitsi, and P. Millié, Chem. Phys. **275**, 75 (2002).

[103] V. May and O. Kühn, *Charge and Energy Transfer Dynamics in Molecular Systems* (Wiley-VCH Verlag GmbH & Co. KGaA, Weinheim, Germany, 2011).

[104] E.P. Kenny and I. Kassal, J. Phys. Chem. B **120**, 25 (2016).

[105] C.-P. Hsu, Z.-Q. You, and H.-C. Chen, J. Phys. Chem. C **112**, 1204 (2008).

[106] C.P. Hsu, Acc. Chem. Res. **42**, 509 (2009).

[107] Y. Shao, Z. Gan, E. Epifanovsky, A.T.B. Gilbert, M. Wormit, J. Kussmann, A.W. Lange, A. Behn, J. Deng, X. Feng, D. Ghosh, M. Goldey, P.R. Horn, L.D. Jacobson, I. Kaliman, R.Z. Khaliullin, T. Kuś, A. Landau, J. Liu, E.I. Proynov, Y.M. Rhee, R.M. Richard, M.A. Rohrdanz, R.P. Steele, E.J. Sundstrom, H.L. Woodcock, P.M. Zimmerman, D. Zuev, B. Albrecht, E. Alguire, B. Austin, G.J.O. Beran, Y.A. Bernard, E. Berquist, K. Brandhorst, K.B. Bravaya, S.T. Brown, D. Casanova, C.-M. Chang, Y. Chen, S.H. Chien, K.D. Closser, D.L. Crittenden, M. Diedenhofen, R.A. DiStasio, H. Do, A.D. Dutoi, R.G. Edgar, S. Fatehi, L. Fusti-Molnar, A. Ghysels, A. Golubeva-Zadorozhnaya, J. Gomes, M.W.D. Hanson-Heine, P.H.P. Harbach, A.W. Hauser, E.G. Hohenstein, Z.C. Holden, T.-C. Jagau, H. Ji, B. Kaduk, K. Khistyaev, J. Kim, J. Kim, R.A. King, P. Klunzinger, D. Kosenkov, T. Kowalczyk, C.M. Krauter, K.U. Lao, A.D. Laurent, K. V. Lawler, S. V. Levchenko, C.Y. Lin, F. Liu, E. Livshits, R.C. Lochan, A. Luenser, P. Manohar, S.F. Manzer, S.-P. Mao, N. Mardirossian, A. V. Marenich, S.A. Maurer, N.J. Mayhall, E. Neuscamman, C.M. Oana, R. Olivares-Amaya, D.P. O'Neill, J.A. Parkhill, T.M. Perrine, R. Peverati, A. Prociuk, D.R. Rehn, E. Rosta, N.J. Russ, S.M. Sharada, S. Sharma, D.W. Small, A. Sodt, T. Stein, D. Stück, Y.-C. Su, A.J.W. Thom, T. Tsuchimochi, V. Vanovschi, L. Vogt, O. Vydrov, T. Wang, M.A. Watson, J. Wenzel, A. White, C.F. Williams, J. Yang, S. Yeganeh, S.R. Yost, Z.-Q. You, I.Y. Zhang, X. Zhang, Y. Zhao, B.R. Brooks, G.K.L. Chan, D.M. Chipman, C.J. Cramer, W.A. Goddard, M.S. Gordon, W.J. Hehre, A. Klamt, H.F. Schaefer, M.W. Schmidt, C.D. Sherrill, D.G. Truhlar, A. Warshel, X. Xu, A. Aspuru-Guzik, R. Baer, A.T. Bell, N.A. Besley, J.-D. Chai, A. Dreuw, B.D. Dunietz, T.R. Furlani, S.R. Gwaltney, C.-P. Hsu, Y. Jung, J. Kong, D.S. Lambrecht, W. Liang, C. Ochsenfeld, V.A. Rassolov, L. V. Slipchenko, J.E. Subotnik, T. Van Voorhis, J.M. Herbert, A.I. Krylov, P.M.W. Gill, and M. Head-Gordon, Mol. Phys.

113, 184 (2015).

[108] J. Gierschner, Y.-S. Huang, B. Van Averbeke, J. Cornil, R.H. Friend, and D. Beljonne, J. Chem. Phys. **130**, 044105 (2009).

[109] A. Sassella, D. Braga, M. Campione, T. Ciabattoni, M. Moret, J. Parravicini, and G.B. Parravicini, J. Appl. Phys. **109**, 013529 (2011).